Simulation of a counter-current horizontal gas/liquid flow experiment at the WENKA channel using a droplet entrainment model

Höhne, T.; Gabriel, S.;

Simulation of a counter-current horizontal gas/liquid flow experiment at the WENKA channel using a droplet entrainment model

Thomas Höhne[1], Stephan Gabriel[2]

[1]Helmholtz-Zentrum Dresden-Rossendorf (HZDR) - Institute of Fluid Dynamics
P.O.Box 510119, D-01314 Dresden, Germany

[2] Karlsruhe Institute of Technologies (KIT), Institute for Nuclear and Energy Technologies (IKET)
Hermann-von-Helmholz-Platz 1, 76344 Eggenstein-Leopoldshafen, Germany

Abstract

One drawback today in simulating horizontal wavy two-phase flows is that there is no treatment of droplet formation mechanisms at the liquid surface. For self-generating waves and slugs, the interfacial momentum exchange and the turbulence parameters have to be modelled correctly. Furthermore, understanding and considering the mechanism of droplet entrainment for heat and mass transfer processes is of great importance in the nuclear industry.

Therefore a step of improvement of modelling liquid/gas interfaces is the consideration of droplet entrainment mechanisms. The proposed entrainment model assumes that due to liquid turbulence the interface gets rough and wavy leading to the formation of droplets. The new approach is validated against existing horizontal two-phase flow data from the WENKA (*Water ENtraninment Channel KArlsruhe*) channel.

Tests were carried out for water and air at ambient pressure and temperature. High speed videometry was applied to obtain velocities from flow pattern maps of the rising and falling fluid. In the horizontal part of the channel with partially reversed flow the fluid velocities were measured by planar particle image velocimetry. The test MP 28 with droplet generation at the reversed flow conditions was utilized to compare it with the simulation data. The agreement of the experimental findings and CFD results is acceptable. Also the droplet mass flow was compared and showed the applicability of the droplet entrainment model. Further work is necessary to validate the model for different flow conditions.

Keywords

CFD, horizontal flow, AIAD, droplet entrainment, two-phase flow, HAWAC, HZDR, OVM, PIV, Isokinetic Sampling Probe, WENKA

Introduction

For heat and mass transfer processes in two-phase flow systems an understanding of the conditions leading to entrainment of a liquid surface film by a gas flow is of considerable practical importance. The mechanisms of mass, momentum, and energy transfer is significantly altered by the inception of entrainment (Ishii et al., 1975). A wavy liquid surface can be entrained into a gas flow in different

ways. Hydrodynamic and surface forces govern the motion and deformation of the wave crests. One example of droplet formations at the wave crest is shown in Fig. 1 for rolling wave flow condition at the WENKA channel.

Fig. 1 Droplet formation at the wave crest (rolling wave flow condition at WENKA channel)

Under certain conditions, these forces lead to an extreme deformation of the interface, which results in the breakup of a portion of a wave into several droplets. The forces acting on the wave crests depend on the surrounding flow pattern as well as on the shape of the interface. Ishii et al. (1975) explain the four basic types of entrainment mechanisms, which are shown in Fig. 2. In the first type the tops of large amplitude roll waves are sheared off from the wave crests by the turbulent gas flow (Hewitt and Hall-Taylor, 1970). The drag force acting on the wave tops deforms the interface against the retaining force of the liquid surface tension. The second type of entrainment is caused by undercutting the liquid film by a gas flow (Hewitt and Hall-Taylor, 1970). The third type is related to the bursting of gas bubbles. It was shown by Newitt et al. (1954) that droplets can be generated by a bubble rising to the surface of a liquid. The fourth type of entrainment is caused by the impingement of liquid droplets or mass to the film interface. Advancing roll-wave fronts may produce small size droplets by this mechanism. All these mechanisms can occur in the case of a Loss Of Coolant Accident (LOCA) in a nuclear reactor. A stratified counter-current two-phase flow establishes through the hot-leg injection. A similar flow can occur in reflux-condenser mode. The experiments in the Upper Plenum Test Facility (UPTF) by Mayinger et.al (1993) have shown that this flow can lead to a Counter Current Flow Limitation (CCFL). This happens if the gas flow rate increases too much and leads to a partially or totally reversed flow of the liquid phase. The phenomenon was studied by various experimental facilities in the past. A review of this has been written by Al Issa and Macian (2011). Siddiqui et. al.
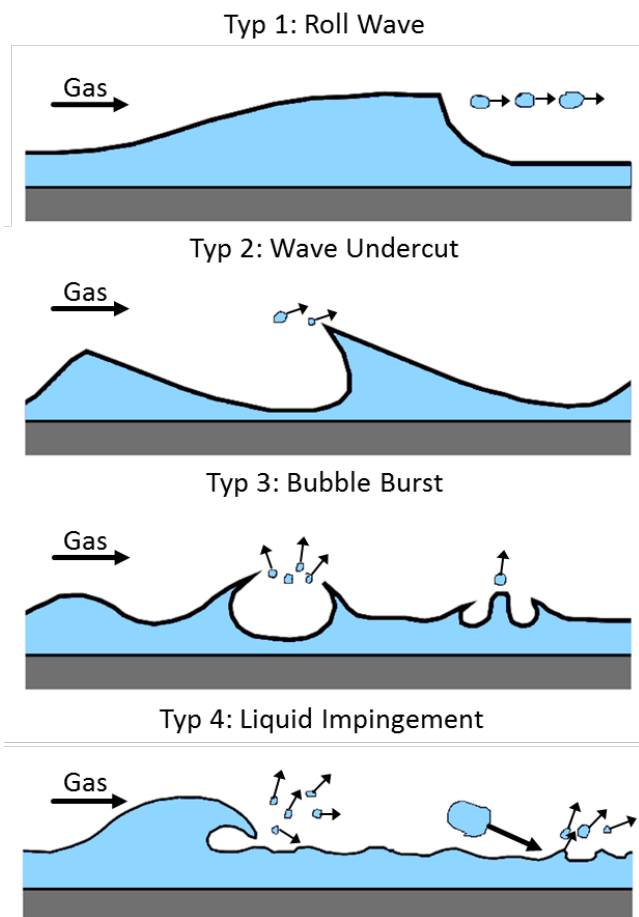

Fig. 2 Different droplet entrainment mechanisms (Ishii, 1975)

(1986) found that CCFL is caused by unstable wave formation at a hydraulic jump. Wang and Kondo (1990) identified the location of the jump near the bend of their channel. Deendarlianto et.al. (2008) and Höhne et.al. (2011) investigated these phenomena in a model of a hot leg of a pressurized water reactor. They analyzed the formation and termination of CCFL dependent on pressure, flow rates and the water level. To accomplish the CCFL phenomena in a bended geometry, CFD codes are a promising approach. For a horizontal channel it was demonstrated by Gargallo (2004), Wintterle (2008) and Stäbler (2007), that it is possible to develop a mechanistic model. To carry this approach to the bended geometry, more experimental data of the local parameters is needed. The most important quantities for model development and validation are the fluid velocities, the void fraction and the pressure drop in the channel.

A further step of improvement of modelling the phenomena using CFD tools is the consideration of droplet entrainment mechanisms. The proposed entrainment model assumes that due to liquid turbulence the interface gets rough and wavy leading to the formation of droplets. The new approach is validated against existing horizontal two-phase flow data from the WENKA channel and will improve the knowledge about droplet entrainment at horizontal counter current flow conditions.

Algebraic Interfacial Area Density Model

The CFD calculation of the WENKA experiment uses the "Algebraic Interfacial Area Density" framework. The AIAD model was developed in close cooperation by ANSYS and HZDR and is described in Yegorov (2004) and Höhne and Mehlhoop (2014).

The basic idea of the AIAD model is:

- The interfacial area density (IAD) allows the detection of the morphological form and the corresponding switch of each correlation from one object pair to another.
- It provides a law for the interfacial area density and the drag coefficient for a full range of phase volume fractions from no liquid to no gas.
- The model improves the physical modelling in the asymptotic limits of bubbly and droplet flows.
- The interfacial area density in the intermediate range is set to the interfacial area density for free surface.

To resolve the interface of continuous gas structures, the interface has to be localized. This is based on a new appropriate blending function Ψ_{surf} (Gauß and Porombka, 2015). It bases on the volume fraction and its gradient and is designed in a generalized form capable for applications describing not only bubble regions but also droplet regions. It replaces the blending taken from the AIAD model (Höhne and Mehlhoop, 2014) which was combined with a volume fraction based interface function in the original GENTOP concept of Hänsch et al. (2012).

The interface blending function is defined as

$$\psi_{Surf} = \varphi_{sf}\left(f_b - f_d\right) \tag{1}$$

which is equal to zero at the interphase boundary. Additionally, it provides information about the morphology:

$$\psi_{Surf} = \begin{cases} 1 & \text{bubble region} \\ 0 & \text{interface} \\ -1 & \text{droplet region} \end{cases}$$

The blending functions for the potentially continuous-phase bubble regime f_b and droplet regime f_d are given by:

$$f_b = \frac{1}{2}\left[1 + \cos\left(\pi \frac{\tilde{\alpha}^G - (\alpha_{b,crit} - \Delta_\alpha)}{2\Delta_\alpha}\right)\right] \tag{2}$$

$$f_d = \frac{1}{2}\left[1 + \cos\left(\pi \frac{\tilde{\alpha}^L - (\alpha_{d,crit} - \Delta_\alpha)}{2\Delta_\alpha}\right)\right] \tag{3}$$

The interface blending function is given by:

$$\varphi_{sf} = \frac{1}{2}\left[1 + \cos\left(\pi \frac{\nabla\tilde{\alpha}^c - (\nabla\alpha_{crit} - \Delta_{\nabla\alpha})}{2\Delta_{\nabla\alpha}}\right)\right] \tag{4}$$

with α_{crit} = 0.3 and $\Delta_{\nabla\alpha}$ = 0.05.

The AIAD model, shown in Höhne (2014), allows detection of morphological form of two phase flow and is able to distinguish between bubbles, droplets and the interface through a corresponding switching via a blending function of each correlation from one object pair to another.

Based on Ψ_{surf} (blending function), formulations for interfacial area density and drag are defined as in eqs. (13) and (14),

$$A_{GasC} = (1 - |\Psi_{surf}|) A_{fs} + a_{sign}|\Psi_{surf}| A_b + (1 - a_{sign})\Psi_{surf}|A_d \tag{5}$$

$$C_{D,GasC} = (1 - |\Psi_{surf}|) C_{D,fs} + a_{sign}|\Psi_{surf}| C_{D,b} + (1 - a_{sign})\Psi_{surf}|C_{D,d} \tag{6}$$

with

$$a_{sign} = \begin{cases} 1 \text{ if } sign(\Psi_{surf}) = 1 \\ 0 \text{ else} \end{cases}.$$

Three different drag coefficients are applied:

1. $C_{D,bubb}$ (for bubbly regions): Ishii and Zuber Drag Formulation
2. $C_{D,drop}$ (for droplet regions): Ishii and Zuber Drag Formulation

$C_{D,fs}$ (for interface region): The drag is ruled by viscous surface stresses and the formulation as proposed by Höhne and Mehlhoop (2014) is used.

$$C_{D,fs} = max\left[0.01, \frac{[\alpha_l \tau_{w,l} + \alpha_{cg} \tau_{w,cg}]}{\rho_m u_{slip}^2}\right] \tag{7}$$

Similarly, the interfacial area density is applied as three different equations:

$A_{D,bubb}$ (based on particle model formulations)

$$A_{D,bubb} = \frac{6\alpha_{cg}}{d_{cg}}$$

(8)

$A_{D,drop}$ (based on particle model formulations)

$$A_{D,drop} = \frac{6\alpha_l}{d_l}$$

(9)

The IAD of the free surface, A_{FS}, is defined as the magnitude of the gradient of the liquid volume fraction α_L, as given in Eq. (5), with $\boldsymbol{n}$ being the normal vector of the free surface.

$$A_{FS} = |\nabla\alpha_L| = \frac{\partial \alpha_L}{\partial n}$$

(10)

The minimum volume fraction of liquid (10^{-7}) is set inside the continuous phase.

Turbulence damping Liquid/GasC

Without any special treatment of the interface, the high velocity gradients at the interface, especially in the gaseous phase, generate levels of turbulence that are too high throughout the two-phase flow when using eddy viscosity models like the k-ε or the k-ω model. Therefore, a certain amount of damping of turbulence is necessary in the region of the interface, because the mesh is too coarse to resolve the velocity gradient in the gas phase at the interface.

For the two-fluid formulation, Egorov (2004) proposed a symmetric damping procedure. This procedure provides a solid wall-like damping of turbulence in both gas and liquid phases. More information can be found in Höhne and Mehlhoop (2014).

Sub-grid wave turbulence Liquid/GasC

Small waves created by Kelvin-Helmholtz instabilities that are smaller than the grid size are neglected in traditional two phase flow CFD simulations, but the influence on the turbulence kinetic energy of the liquid side can be significantly large.

The consequence of the specific turbulent kinetic energy k_{SWT} is prescribed in a source term where the gradients of the local velocities and the liquid density are present and which is added to the total turbulent kinetic energy k (Wilcox, 1994). More information about the sub-grid wave turbulence is found in Höhne and Mehlhoop (2014).

The droplet entrainment model

In order to find a universal entrainment model, some assumptions have to be made. The proposed entrainment model assumes that due to liquid turbulence the interface gets rough and wavy and forms bulbs with an average size of *a(x)* (see Fig. 3). All droplet formations occur in a layer close to the interface, which has a thickness of C_1a. The rate of droplet formation is estimated by the quantity of liquid passing an interfacial layer relative to the velocity of the interface: Consequently, the liquid film is forming a droplet only if the water bulb moves upward into the gas phase relative to the

interface. The roughness is estimated in Fig. 4 as a = C2k/g with k(x) being the local liquid turbulent kinetic energy including the sub-grid wave turbulence.

Using this approximation leads to a local deposition rate:

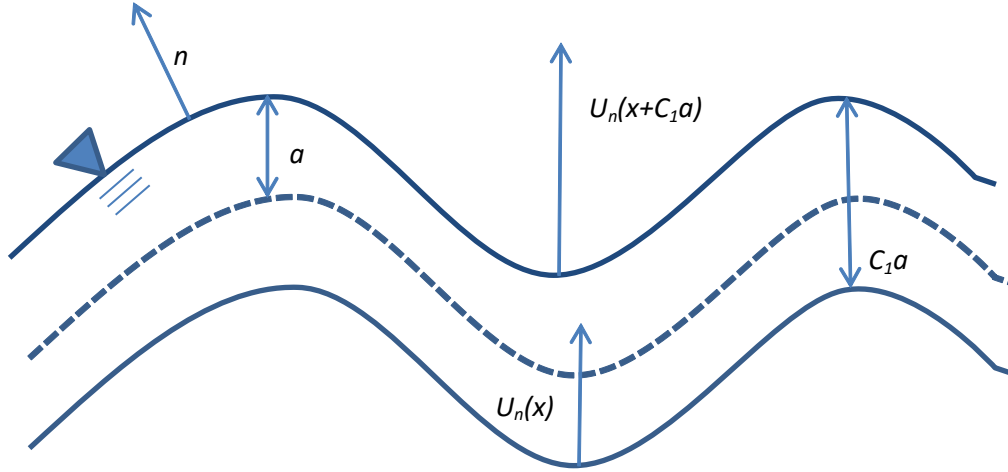$$d(x) = \frac{C_{Drop}}{g} k(x) \frac{\partial u_n}{\partial n}(x) \qquad (11)$$

Fig. 3 Schematic diagram on droplet entrainment (similar to Ma et al., 2011)

with $C_{Drop} = C_1 C_2$ as a new constant. The parameter C_{Drop} is left undetermined and should depend on the fluid pair properties. The created droplets are then distributed as a volume source at the interface in a layer, which is ϕ_{Drop} thick. Therefore, the droplet formation rate per unit volume and time is:

$$D(x) = \frac{C_{Drop}}{g\phi_{Drop}} k(x) \frac{\partial u_n}{\partial n}(x) \qquad (12)$$

The rate (Eq. 12) is essentially determined by two local key variables: the turbulent kinetic energy and the outward velocity gradient. On the other hand if droplets occur below the water surface a complete coalescence should lead to a mass transfer of the droplets into the continuous liquid phase. This is prescribed in the following continuity source/sink term:

$$\dot{m}_{dl \to cl}(x) = f_B \cdot \alpha_{Drop} \cdot \rho_{liq}/\Delta t \qquad (13)$$

Ma et al. (2011) describes a similar model for air entrainment. He calculates the position of the surface using a single-phase level-set function. Later on in a second step the entrainment is calculated as a volume source using the two-fluid model. In doing this, the description was restricted to mono-dispersed bubbles and one-way coupling ignoring the effect of the gas phase on the liquid.

Table 1: Model settings

AIAD
Focus: Droplets
C_1=2
$a= C_2k/g=2\Delta x$
$\Phi_{Drop}=C_1a=4\Delta x$ (grid size dependent)
$C_{Drop}=2C_2$

Another way to interpret this entrainment model is also indicated by Ma et al. (2011) and considers an incompressible liquid phase. This implies that $\frac{\partial u_n}{\partial n} = -\nabla_s \cdot u_s$ leading to an entrainment criteria of a negative surface divergence. This model idea corresponds to the way the sub-grid waves are modeled using the model of Brocchini and Peregrine (2001).

While the model of Ma et al. (2011) is assuming the formation process occurring in a thin layer underneath the free surface, in our case this layer is supposed to be the thickness of smeared interface, that we defined to be $\Phi_{Drop}=C_1a=4\Delta x$ (see Table 1 grid size dependent). With *k(x)* appearing in the equation, the droplet formation is directly connected to the sub-grid wave turbulence described in the previous section.

Table 2: Modeling the different phases

	Water	Droplets	Air
Morphology	Continuous Fluid	Dispersed Fluid	Continuous Fluid
Turbulence model	k-ω	Zero equation	k-ω
Turbulence Damping	x	-	x
Sub-grid wave turbulence SWT	x	-	-
Droplet entrainment	- m drop	m drop	-
Complete coalescence	m coal	-m coal	-

Table 3: Fluid pair settings

Fluid Pair	Air at 25 C | Droplets	Air at 25 C | Water	Droplets | Water
Interphase transfer model	Particle Model	Mixture Model AIAD	Particle Model
Momentum transfer	Ishii Zuber (1979)	Höhne (2014)	Ishii Zuber (1979)

For the concept the volume source of the created droplets should only be activated within the detected free surface region using the function f_{FS}. A new dispersed phase "droplet" with the material properties of the liquid phase and a uniform mean diameter is added in the multi-fluid AIAD framework to the gas and the liquid phase to form a three-phase flow. The mass of the dispersed

liquid "droplet" is defined as a continuity source for dispersed water respectively sinks for the continuous water in the form of:

$$m_{Drop}(x) = f_{FS}\rho_l\alpha_l D(x) \tag{14}$$

$$D_{Drop}(x) = \frac{C_{Drop}}{4\Delta xg}k_l(x)\frac{\partial u_{l,n}}{\partial n}(x) \tag{15}$$

The parameter C_2 in Table 1 is left undetermined and is set to 0.01 in the first CFD simulation. It should depend on the fluid pair properties. First verification and validation of the droplet entrainment model using C$_2$=0.01 was done in Höhne et al. (2015) and Höhne and Hänsch (2015).

A second simulation was done with C_2 =0.1 and compared to the experimental findings.

The experimental facility

The WENKA facility, is a channel constructed to observe stratified counter-current two phase flows. Water and air, instead of steam, are used for the experiments. Gargallo (2004) and Stäbler (2007) studied the flow phenomena in a horizontal channel. It was noted that the transition from supercritical to subcritical flow through a hydraulic jump is a precondition for flooding occurrence. To observe the flow phenomena near the hydraulic jump, the bent channel in Fig. 4 is used. The channel has a cross section of 90 × 110 mm². The angle of the inclined section is 45° with a vertical heigt difference of 430 mm.
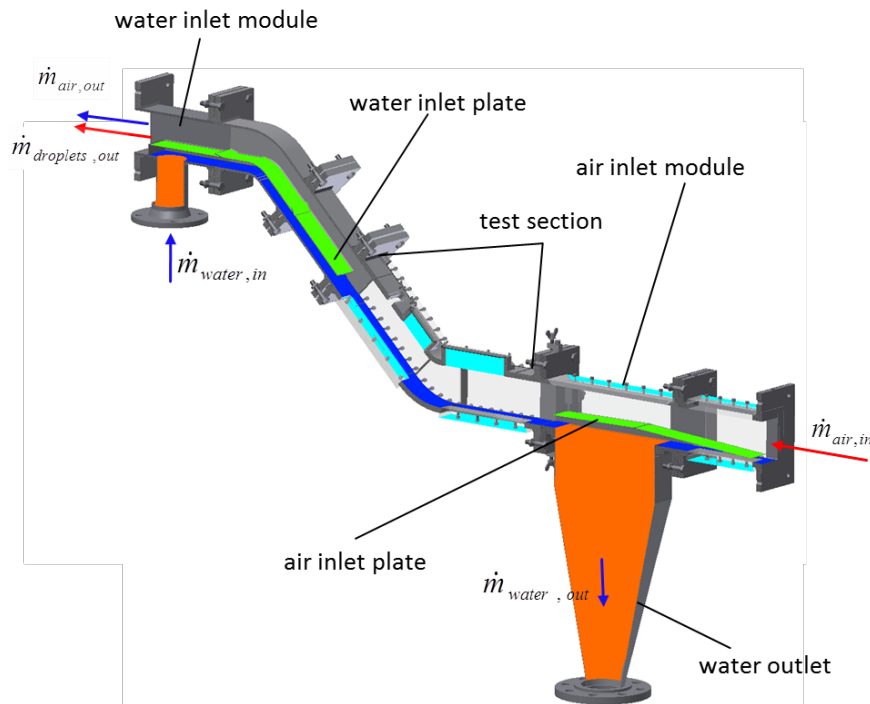

Fig. 4. Test section and inlet sections for water and air

The water inlet plate in the inclined part is fixed but the air inlet plate is adjustable. The air is fed into the channel by a blower, through a honeycomb structure, and through an inlet tube 1.43 m long,

which is connected to the air inlet section. The air flow profile is fully developed before it enters the test section, as confirmed by local measurements. The air leaves the channel into a cyclone which is connected upstream. The counter-current flow of water is pumped into the channel and moves under the water inlet plate into the test section. It accelerates at the inclined part, passes the horizontal part and leaves the channel through the chute under the air inlet plate. The length of the horizontal part is 290 mm. The most important design parameters are summarized in Table 3. The channel allows nearly full optical access to the test section through elements made of acrylic glass on the sides and at the bottom. On the top, there are several slots to attach different probes or inject a laser light sheet for optic measurements. The boundary conditions like fluid temperature and barometric pressure are measured by several thermocouples and pressure sensors in the loop.

Table 3: Design features of the WENKA facility

Design features of the WENKA facility parameter	value	unit
Cross section h × d	90 × 110	mm²
angle	45°	-
vertical height	430	mm
Length of the horizontal part	290/510	mm
superficial air velocity	7.0 –30.0	m/s
superficial water velocity	0.025 –0.16	m/s

The flow regime in the channel is influenced by numerous flow parameters and fluid properties. For example the mass flows of both fluids, the viscosities and the surface tension. Depending on the flow ratio of air and water, which are the most important parameters, different flow regimes occur in the test section. Fig. 5 shows a flow pattern map for increasing and decreasing airflows. Four flow patterns can be distinguished from each other, going from the supercritical flow to the fully reversed flow. At low air flow rates, a stable supercritical countercurrent flow occurs in the channel (Froude-Number < 1). Increasing the air flow leads to a stronger momentum exchange between the fluids. Onset of droplet entrainment and the occurrence of a hydraulic jump in the bent with a subcritical water flow behind it can be the consequence. Once a hydraulic jump occurs, air bubbles are mixed into the water flow. However, the decreasing water velocity and the intermixing of bubbles lead then to a higher water level in the horizontal part of the test section. As a result, the continuous air flow above the liquid surface is accelerated and the momentum exchange is intensified. Therefore, the flow map for decreasing air flow (Fig. 5 right) shows a hysteresis in the flow regime of partially reversed flow.
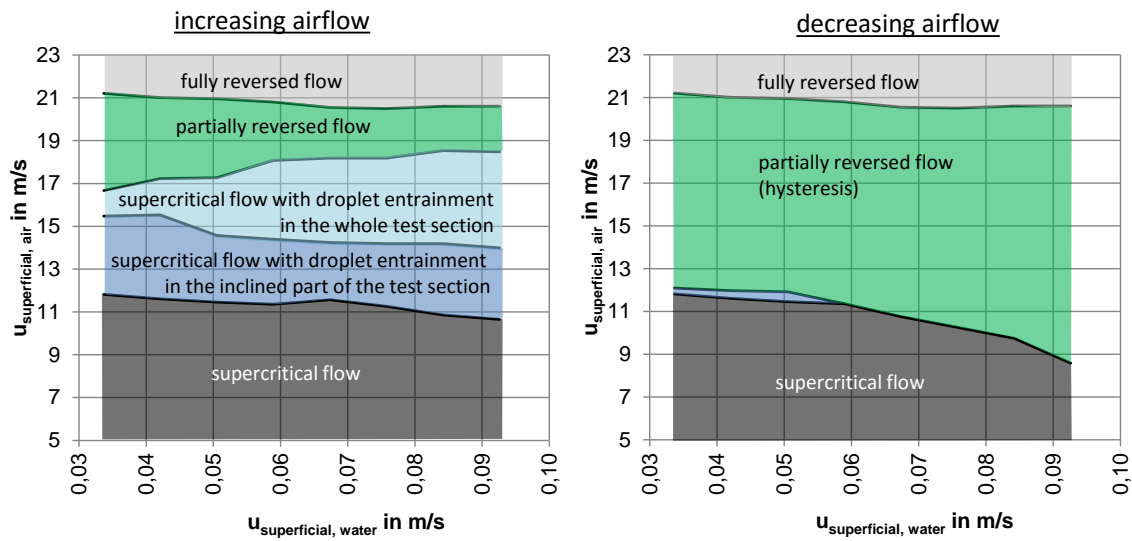
T. Höhne, S. Gabriel

Fig. 5. Flow pattern maps in the horizontal part of the test section for increasing and decreasing air flow rate

For the measurements, five measuring sites were defined in the channel at which local flow parameters were determined. Fig. 5 illustrates the location of the measurement sites at the channel. The measurement plane was in the middle of the channel so the side walls had less influence on the flow.
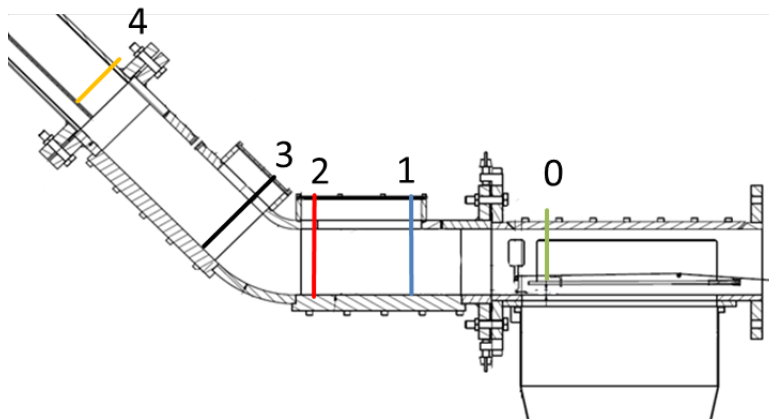

Fig. 6. Measurement sites in the WENKA Test section.

Describing the flow conditions by numerical models within a CFD-Code, it is essential to obtain local experimental data. Therefore it is necessary to measure physical quantities locally in the channel by advanced measurement techniques.

Measurement technique

The two most important quantities for model development in CCFL are the time averaged void fraction and the time averaged local fluid velocities. Both were measured in the WENKA facility. Concerning accuracy, non-intrusive measurement methods were preferred. A videometric method

for void measurement was developed and validated. The fluid velocities were taken by planar particle image velocimetry (PIV).
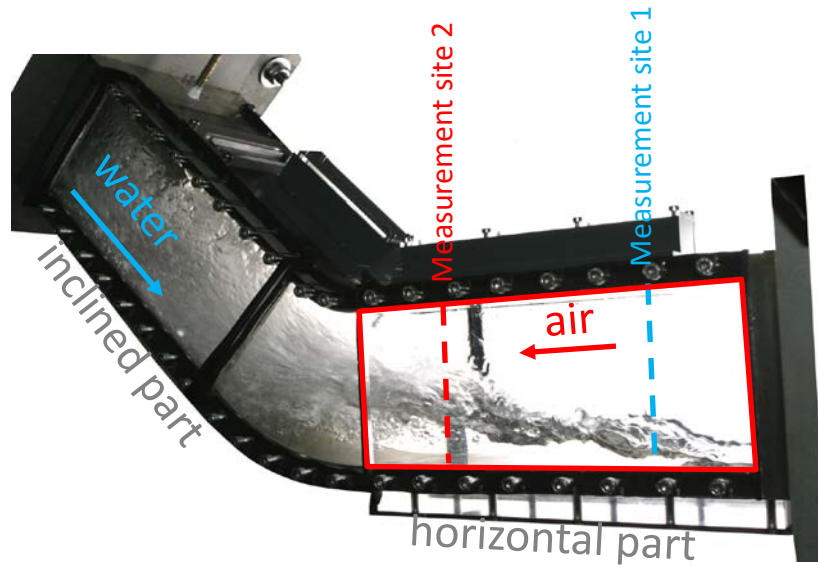

Fig. 7. Test section with partial reversed flow at v_L=0.042m/s and v_G= 15.15 m/s (hysteresis zone)

Void fraction

For the development of CFD-models high resolution data for the phase distribution is needed. There are only a few measuring instruments which are suitable for this purpose. For example the fast electrons beam X-ray tomography (Fischer and Hampel, 2009, Havel et. al. 1996) or wire-mesh sensors (Prasser et al,. 1998).
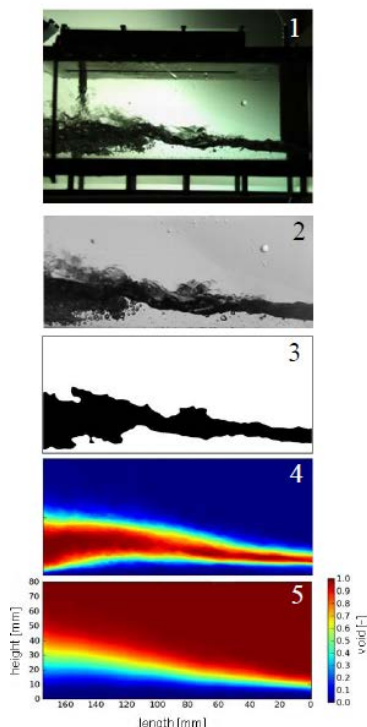

Fig. 8. Videometric void measurement sequence

Due to the good optical accessibility of the test, an optical measuring method is suitable. The design of the WENKA channel provides a good optical access to the flow. Vallée developed already a videometric procedure that allows the detection of the interface in a stratified flow by image processing (Vallée, 2010). With a similar approach, it was possible to develop a videometric measurement method with a huge spatial resolution. A detailed description of this measurement method is given in Gabriel and Kaiser (2017). The measurement method is based image processing of shadow images with a programm implemented in the program language Python. Fig. 8 shows the process in a sequence of five images. The first image (Fig. 8.1) illustrates an original raw image from a sequence of more than 2000 images, which were made by a calibrated camera. The single phase areas are lighter than two phase areas, caused by optical refraction and reflection. In the first step (Fig. 8.2) the image is cut out and a background image is subtracted. The picture is then binariesed by an intensity threshold and small objects are deleted by the morphological functions binary erosion and binary dilation (Fig. 8.3). After this the single images are averaged. The false colored

11

result image (Fig. 8.4) shows the time averaged value of the probability that a two-phase flow was detected. If this image is integrated column wise from the bottom to the top and normalized with the maximum value, Fig. 8.5 is the result. The false colored image shows areas with pure air in red and areas with pure water in blue. The transition in between is the probability that air was detected, which we call the void fraction. For comparison with CFD-data, it is possible to read out single pixel values or complete columns to plot it in a diagram. A summary of the measurement parameters is shown in Table 5.

Table 5 Void fraction measurement parameters

Quantity	Value	Unit
spatial resolution	1007 × 444 / 83 × 188	Pixel / mm
time resolution	100	Images/Second
number of greyscale values	256	-
number of analyzed Images	2448	-

The validation of this new void measurement method was done by simultaneous measurements with the single tip conductivity probe of Stäbler (2007) in comparison with the videometric method. At low void values the videometric method overrates the void fraction measured by the conductivity probe. At higher void values it is underestimated. This uncertainty can have multiple sources. Obvious reasons are perspective errors, which take place when the image does not exactly show a horizontal projection of the two phase area. Other sources of errors are bubbles and droplets, because they are only detected by the conductivity probe if they are in a direct electrical contact with the channel. Additionally, the conductivity probe has a contact hysteresis which leads to an error of 1%. Another source of error of the videometric method is the channel depth which should be small to minimize 3D effects. Altogether, the validation shows a averaged measurement uncertainty of 8,5% . Compared with other local void measurements, this error is considered to be acceptable. The error bars in the following diagrams correspond to the standard deviation over the evaluation of 10 sequences with 4900 images each.

Velocities and turbulence kinetic energy

The fluid velocities and related quantities like RMS-values or turbulent kinetic energy were measured by the well-known method Particle Image Velocimetry (PIV). The system consists of a Nd:YAG laser a CCD camera and the timing unit in the measuring computer. The liquid phase was illuminated from below and the gas phase from above with a laser light sheet. The camera is attached sideways with a horizontal view into the channel. The measurement plane is located in the middle of the channel. Due to the numerous drops and bubbles in the turbulent flow, it is not always possible to produce usable particle images of this turbulent two-phase flow. Reflection and refraction of the laser light sheet in the dispersed phase leads to glare effects and disturb the measurement. Therefore fluorescent particles of Rhodamine-B doped PMMA particles were used as seeding particles in water. The green illumination (532 nm) from the laser causes red fluoresce by the particles. If the Camera is equipped with an optical bandpass filter for red light (> 612 nm) only the fluorescent signal can reach the sensor chip. Signals due to reflections at the liquid interface have a significantly lower intensity and can therefore be eliminated in the evaluation due to their brightness. This ensures that only signals from the laser's measuring plane are evaluated. In this way, local velocity can be measured in water up to a very high proportion of bubbles. However, measurement uncertainty increases with increasing void, because the number measurement values decreases with increasing void fraction.

Within this work, it was not possible to find a suitable fluorescent tracer for measurements in gaseous phase. Therefore, a non-fluorescent oil was used in the experiments. The measurement uncertainties that occurred during these experiments are not negligible, so measurements based on the pure gas phase (measuring site 0) must be used. The error bars in the following diagrams correspond to the 95% confidence interval.

Droplet Mass Flow rate

As a further important flow variable, the droplet mass flow has been measured. Two-phase flows with a high droplet mass flow rate are not accessible for optical measurement techniques due to the refraction on the liquid interface. Therefore an isokinetic sampling probe with an inlet cross section of 10×12 mm² was used. The device consists of the probe tip for sampling, a cyclone for droplet separation, a flow meter for air and water as well as a water tank and a fan that drives the system (Fig. 9). After sampling, air and water are separated in a cyclone and the mass flows of both phases are measured using conventional flow meters.

The isokinetic behavior of this system is an important precondition for reliable results. A realistic droplet mass flow rate can only be measured if the flow field of the channel is not disturbed due to the sampling device. If the probe extracts too much or not enough fluid, the measured droplet mass flow rate is overestimated or underestimated. Therefore it is adjusted in such a way, that the flow velocity in the probe exactly corresponds to the undisturbed flow velocity in the channel. Then the flow in the channel remains virtually undisturbed at the measurement site. The probe is adjusted by measurement of the static pressure difference inside/outside. Theoretically, the suction velocity is equal to the flow velocity in the channel when static pressure difference disappears. Practically, a slight deviation from this condition is caused by the material cross-section of the sampling probe. Therefore the probe was calibrated by simultaneous PIV measurements at the measurement site. In order to measure a profile the sensor head is traversed in the channel along the vertical coordinate.
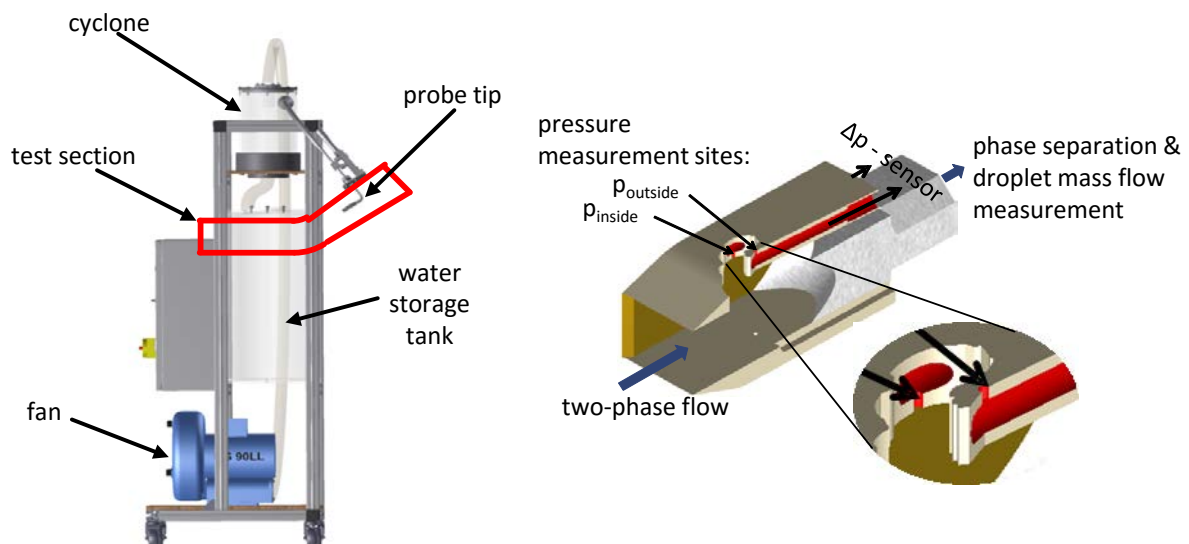

Fig. 9 Probe tip and CAD-model of the isokinetic probe

Thus, the probe takes a representative sample and evaluates the water content of the flow. In the ideal case, the only droplets detected are those whose trajectory is directed into the inlet cross-section of the sensor. However, the flow field of a real, turbulent two phase flow can only be

approximated by a stationary controlled probe. Therefore in addition to isokinetic measurements, hypokinetic and hyperkinetic measurements were made to estimate the inevitable upcoming measurement errors. The value of the potentially isokinetic measurement condition is specified as the measurement result. The measurement results with too high and too low suction rate were used to create the uncertainty bars.

The experiment MP28

In a comprehensive series of measurements, 31 measuring points were examined at WENKA facility in the bent channel. Water mass flow and air mass flow were varied. In the following measurement conditions and results of measuring point 28 are shown. This measuring point was chosen for comparison with the model, because in the flow regime of the partial reversed flow drops, bubbles and waves occur and thus the phase interactions are visible. The boundary conditions of this experiment are shown in Table 7.

Table 6 Boundary conditions of MP28

Quantity	Value	Unit
Water flow	0,42	l/s
Water superficial velocity	0.042	m/s
Air flow	145	l/s
Air superficial velocity	14.6	m/s
Temperature (air/water)	≈20°C	
Pressure	≈1013	mbar

The water flow is supercritical in the inclined part (Froude-Number < 1) and subcritical in the horizontal part of the channel (Froude-Number < 1). The transition between supercritical and subcritical happens in a hydraulic jump near the lower bend. Fig. 10a) shows a snapshot of the flow in the horizontal part of the channel. A large two phase area occurs there under these flow conditions. Many droplets and bubbles can be seen in the continuous liquid and gas phases. In addition to smaller capillary waves, larger gravitational waves can also be seen. The flow is very unsteady and turbulent. The time averaged Void distribution in Fig. 10b) shows that the two-phase area grows from right to left. This is caused by the growth of the waves and the increasing droplet and bubble entrainment near the hydraulic jump.
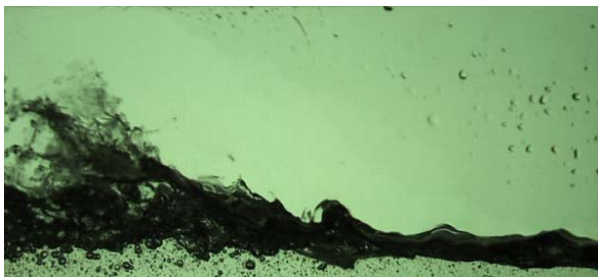

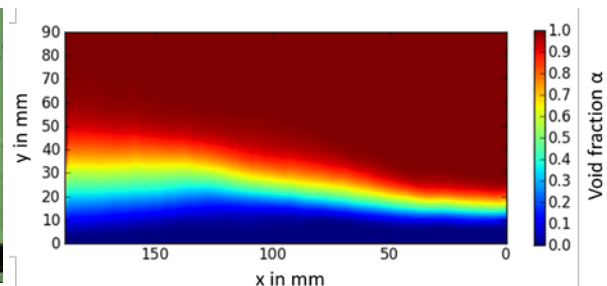**Fig. 10a** Flow picture   **Fig. 10b** Averaged void fraction

In Experiment 28, numerous measurements were carried out at 5 different measuring sites. Due to the limited optical accessibility in the inclined part of the test section it wasn't possible to measure a

velocity or void distribution. There are so many droplets refracting the light that the measurement plane is completely inaccessible for OVM and PIV at this measuring sites.

The simulation setup

The droplet entrainment approach was implemented via the command language CCL into ANSYS CFX-18, 2017. An Euler-Euler multiphase model using fluid dependent RANS k-ω turbulence models was applied. The high-resolution discretization scheme was used for convection terms in the equations. For time integration, the fully implicit second order backward Euler method was applied with a constant time step of Δt = 0.001 s and a maximum of 30 coefficient loops per time-step. Convergence was defined in terms of the RMS values of the residuals, which was less than 10^{-4} most of the time. An initial calculation was done to establish the water level for the entire model length. The inlet conditions are given by both superficial velocities, a pressure distribution is set at the channel outlet.
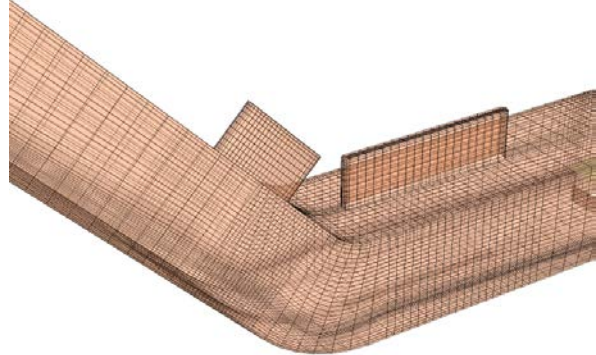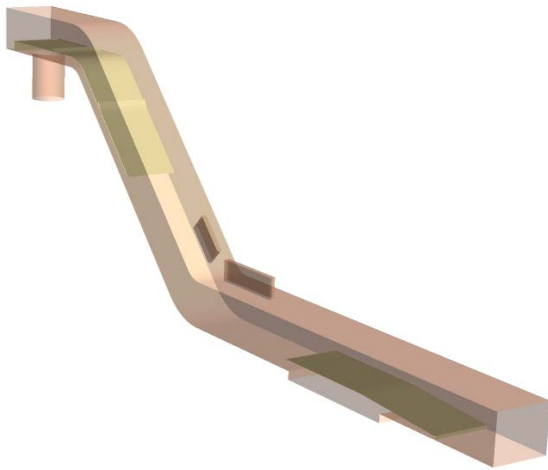

Fig. 11 Modelled geometry of WENKA test facility

Fig. 12 Details of the grid

The grid consists of 1.2×10^{6} hexahedral elements (Figs. 11 and 12).

In the simulation, both phases have been treated as isothermal and incompressible, at 25°C and at a reference pressure of 1 bar. A hydrostatic pressure was assumed for the liquid phase. At the inlet, the turbulence properties were set using the "Medium intensity and Eddy viscosity ratio" option of the flow solver. This is equivalent to a turbulence intensity of 5% in both phases. The inner surface of the channel walls are defined as hydraulically smooth with a non-slip boundary condition applied to both gaseous and liquid phases. The channel outlet was modelled with a pressure controlled outlet boundary condition.

The parallel transient calculation of 30.0 s of simulation time on 32 processors took 16 CPU days. The simulations were run on the HZDR Linux-Cluster hydra4. The cluster consists of two heads and 72 compute nodes. Each node has 2 Intel CPUs (Xeon 8-Core or 16-Core). In general hydra consists of more than 1500 CPU-cores and 8,5 TB of main memory. The network is a 1GbE Ethernet and additionally an InfiniBand fabric with a bandwidth of 40 Gbit/s, which qualifies hydra for sequential,

coarse granularity parallel and massively parallel jobs. The operating system is Ubuntu Linux. The theoretical general peak performance (single precision) amounts to 70,5 TFlop/s.

The simulation package *ANSYS CFX* (2017) was utilized.

ANSYS CFX is an element-based finite-volume method with second-order discretisation schemes in space and time. It uses a coupled algebraic multigrid algorithm to solve the linear systems arising from discretisation. The discretisation schemes and the multigrid solver are scalably parallelized.
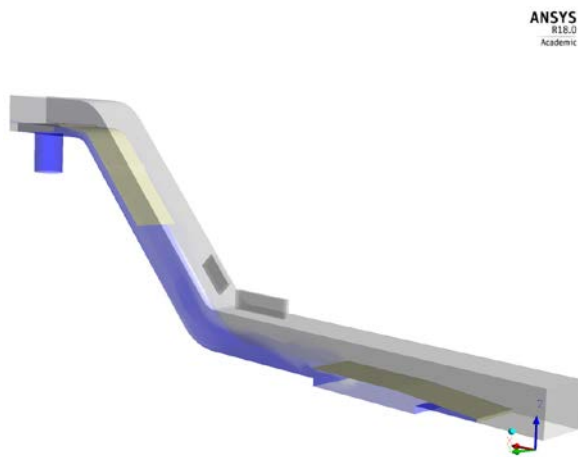
Results

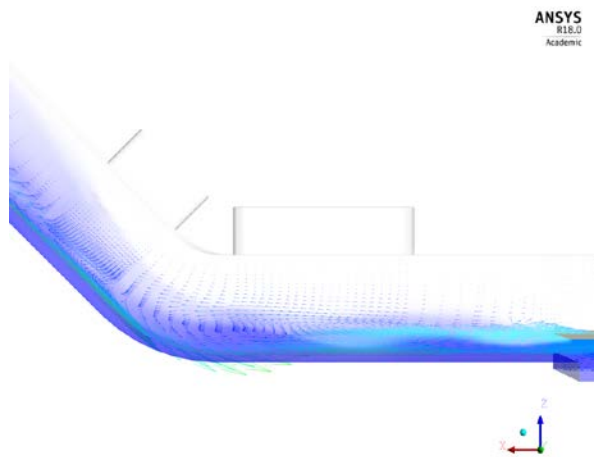**Fig. 13** Flow conditions at 7s after start of simulation

Fig. 14 Superficial water velocity at 7s
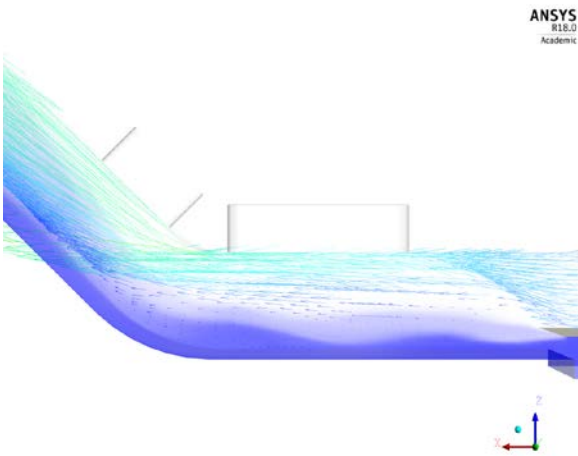

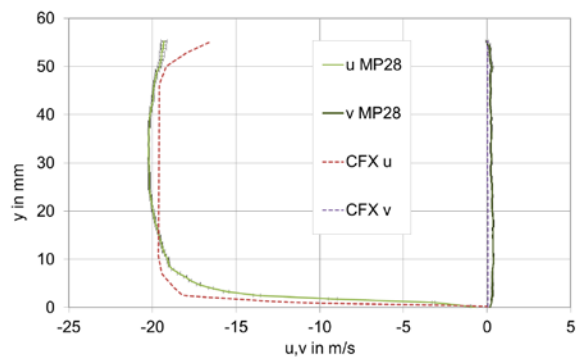**Fig. 15** Superficial air velocity at 7s

Fig. 16 Air u and v velocity profile at Ms0
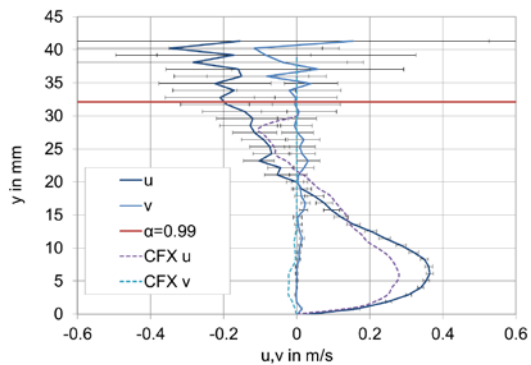

Fig. 17 Water u and v velocity profile at Ms1
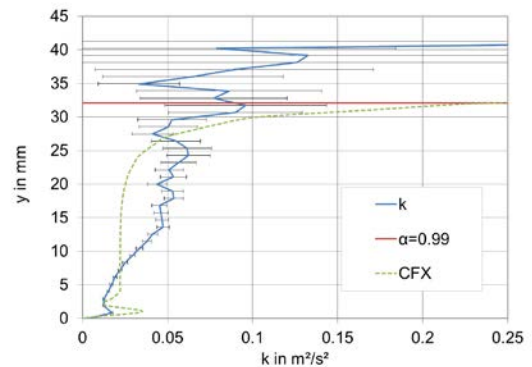

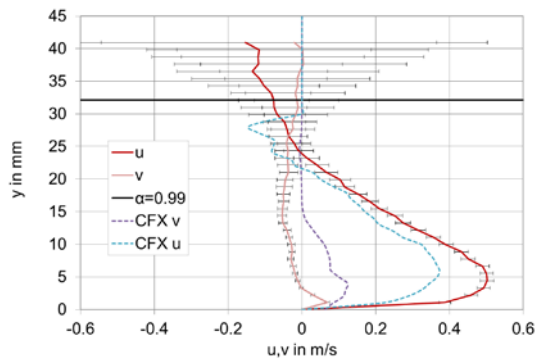**Fig. 18** Turbulence kinetic energy profile at Ms1

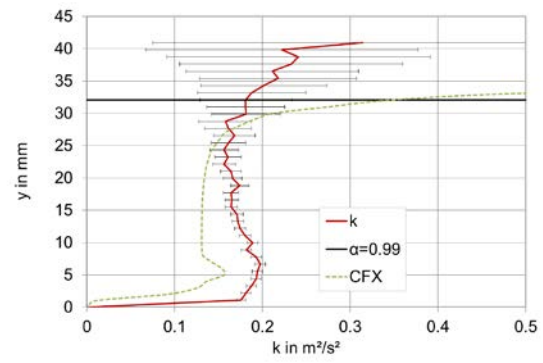**Fig. 19** Water u and v velocity profile at Ms2

Fig. 20 Turbulence kinetic energy profile at Ms1
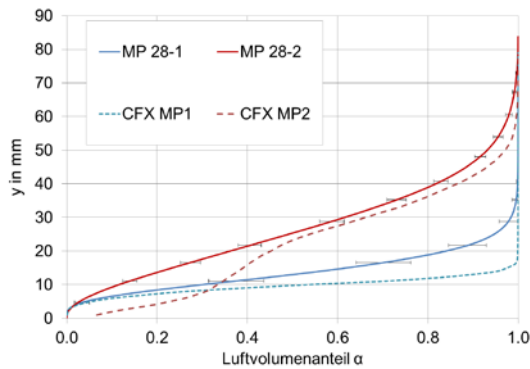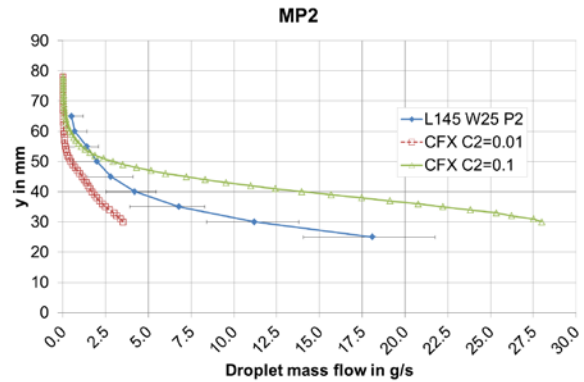

Fig. 21 Air volume fraction at Ms1 and Ms2

Fig. 22 Droplet mass flow (CFX calculation with C2=0.01 and C2=0.1)

If the air volume flow density is increased above 19 m/s, an inverse flow is observed in the channel. The main features of this flow are the changing of the flow direction of a part of the continuous liquid phase, as well as the formation of drops and bubbles. Through the strong wave movements and the droplet inception no air velocities could be measured in the test section. The error bars show the standard deviation between ten evaluated image sequences. The Figs. 13-15 show the CFD results of this reversed flow conditions. Fig. 13 shows the air and water (blue) volume fraction distributions whole test modelled test section. Figs. 14 and 15 show the superficial velocities at the elbow region.

The velocity profile of the incoming air at position 0 (Fig. 16) shows no substantial changes compared to the profiles of the co-current flows. The calculated values are in good agreement with the measured ones. The slightly larger boundary layer in the experiment may occur due to the small edge between the flanges.

The velocities and turbulent kinetic energy of the liquid phase of Ms1 and Ms2 are plotted in the Figures 17-20. They were measured with Particle Image Velocimetry (PIV) and could be shown by the use of fluorescent tracers.

At the measuring site Ms1 the velocity u shows an approximately parabolic profile, with a maximum of about 0.35 m/s. The velocity increases, going from the channel floor, up to a channel height of just under 5 mm. It sinks again, down to zero at the height of y = 20 mm. At this height, the water volume fraction corresponding to Fig. 17 already is less than 90%. The negative velocity increases in the range of 20 mm <y <32 mm with increasing height. At y = 32 mm the air fraction reaches 99%. The

18

measured values above this cannot be regarded as representative for the flow. The time averaged velocity profile of the CFD calculation (Fig. 17) shows a similar behavior. Differences occur in the maximum value (0.28 m/s) and in general above y=28 mm. Due to the very small water volume fraction the superficial water velocity goes to zero.

The measured and calculated vertical velocity components have values close to zero.

The turbulent kinetic energy k has maximum values in the interface region at low liquid fractions α = 90%. The confidence intervals are quite low only for high water content. The calculated values of k have a peak at the channel bottom and also tend to increase drastically close to the interface.

At the measuring site Ms2 the velocity u shows a similar profile compared to Ms1, with a maximum of about 0.5 m/s. The velocity increases, going from the channel floor, up to a channel height of just under 5 mm. It sinks again, down to zero at the height of y = 24 mm. At this height, the water volume fraction corresponding to Fig. 19 is already less than 90%. The negative velocity increases in the range of 24 mm <y <32 mm with increasing height. At y = 32 mm the air fraction reaches 99%. Also in Ms2 the measured values above this cannot be regarded anymore as representative. The time averaged velocity profile of the CFD calculation (Fig. 19) shows a similar behavior. Differences occur in the maximum value (0.38 m/s) and in general above y=23 mm. Due to the very small water volume fraction the superficial water velocity goes to zero.

The measured and time averaged calculated vertical velocity components have small values. However the measured values are positive with a small peak close to the channel bottom and with increasing height they are getting negative. In contrast the CFD results show positive values in the lower channel part and values close to zero further above.

The measured turbulent kinetic energy k (Fig. 20) has maximum values in the interface region at low liquid fractions α = 90%. The confidence intervals are quite low only in high water content and very high in the gas phase. The time averaged values of k (CFD calculation) have a peak at the channel bottom. They also tend to increase drastically close to the interface. The agreement between experiment and calculation is better than at Ms1.

Fig. 21 shows the time averaged measured and calculated air volume fraction at Ms1 and Ms2. The agreement of the experiment and the CFD results is quite good. In general, the mixed region is increasing at Ms2 compared to Ms1.

The droplet mass flow was measured at measuring site Ms2. Fig. 22 shows the results of these investigations. Along the height coordinate at the lowest points one can find the highest droplet mass flow rates. The error bars are made up of the standard deviation (measured value scatter), the measuring error of the pressure measurement and the discretization error of the evaluation. The measurement uncertainty becomes smaller as the height increases both the measured fluctuations as well as the error caused by the pressure measurements decreasing drop volume flow density. Two CFD calculations were carried out. The only difference was that the constant C2 in eq. 12 was modified. The standard value is 0.01. The modified value was increased to 0.1. The droplet mass flow rate was calculated from the droplet superficial velocity the droplet volume fraction per channel segment volume. Fig. 22 shows that the measured droplet mass flow rate lies in between the

calculated C2 values. Further work is necessary to adjust the parameter and to validate the droplet entrainment model.

Summary and Outlook

Understanding the mechanism of droplet entrainment for heat and mass transfer processes is of great importance for horizontal segregated flows. Therefore, a droplet entrainment model inside the AIAD framework was suggested. The entrainment model assumes that due to liquid turbulence the interface gets rough and wavy forming droplets wherever the liquid passes the interfacial region relative to the interface velocity.

The WENKA facility was built up to observe counter-current stratified flow under ambient conditions. The modular design of the channel allows modifications of the geometrical boundary conditions. The optical access permits the dedication of optical and laser-optical measurement methods. A new void measurement method was developed.

The results of the experiments in the flow regime of partially reversed flow show that the two phase area is growing with decreasing distance to the bend. The reversed flow region is smaller at positions near the air inlet section. The velocity fluctuations are growing with the void. All in all, partially reversed flow is a very dynamic, wavy and pulsing flow. In order to reduce the measurement uncertainty in this type of flow and to resolve all effects in detail, the used measurement techniques must be currently developed.

The CFD calculation showed a similar flow behavior compared to the experiments. The droplet entrainment model was validated and adjusted. The droplet mass flow rate is in the range of the observed one.

More verification and validation of the approach is necessary, for which more CFD grade experimental data are required, especially for the validation of droplet entrainment mechanisms.

Nomenclature

A	Interfacial area density (1/m)
A_{Ave}	Average cross sectional area (m^2)
α	Volume fraction
C_D	Drag coefficient
c	Critical velocity (m/s)
d	Diameter (m)
F	Force (N)
g	Constant of gravity acceleration (m/s^2)
h	height (m)
k	Turbulent kinetic energy (m^2/s^2)

L	Length scale (m)
μ	Dynamic viscosity (Pa·s)
n	normal vector of the interface
ν	Kinematic viscosity (m^2/s)
P	Pressure (Pa)
Pr	Prandtl number
q	Turbulent velocity (m/s)
Re	Reynolds number
ρ	Density (kg/m^3)
$S_{i,j}$	Strain rate
σ	Surface tension coefficient of the fluid (N/m)
t	Time (s)
T	Temperature (K)
Tu	Turbulence intensity
τ	Shear stress (Pa)
U	Slip velocity (m/s)
$\dot{V}$	Volumetric flow rate (m^3/s)
u, v, w	Velocity in x, y, z-direction (m/s)
f	Blending function
P	Production term turbulent kinetic energy (m^2/s^2)
q	Turbulent velocity (m^2/s^2)
d	Local deposition rate (m/s)
D	Droplet formation rate per unit volume and time (1/s)
C	Constant
Φ	Interface layer (m)
a	Surface roughness (m)

Subscript

B	Bubble
D	Drop

c	Channel
FS	Free surface
G	Gas
i	Phase index
L	Liquid
l	Lower boundary
s	Superficial
SWT	Sub-grid wave turbulence
t	Turbulent
u	Upper boundary
W	Wall

References

Al Issa, S. and Macian, R. "A review of CCFL phenomenon", Annals of Nuclear Energy, 38, 1795-1819 (2011)

ANSYS CFX, 2017. User Manual. Ansys Inc.

Brocchini, M., Peregrine, D. H. 2001, The dynamics of strong turbulence at free surfaces. Part1. Description, J. Fluid Mech., 449, pp. 225-254.

Deendarlianto, C. Vallée, D. Lucas, M. Beyer, H. Pietruske and H. Carl, "Experimental study on the air/water counter-current flow limitation in a model of the hot leg of a pressurized water reactor," Nuclear Engeneering and Design, 238, 3389-3402 (2008)

Fischer, F. and Hampel, U. 2010 "Ultra fast electron beam X-ray computed tomography for two-phase flow measurement". Nuclear Engineering and Design, Vol. 240, pp. 2254-2259.

Gabriel, S., Experimentelle Untersuchung der Tropfenabscheidung einer horizontalen, entgegengerichteten Wasser/Luft-Schichtenströmung, Dissertation, KIT-Scientiffic, Reports 7683, (2014)

Gabriel, S., Kaiser, F. et. al., optical void measurement method for stratified wavy two phase flows, Proceedings of 9th World Conference on Experimental Heat Transfer, Fluid Mechanics and Thermodynamics, Iguassu Falls, Brasil (2017)

Gargallo, M., "Countercurrent Flow Limitations in Horizontal Stratified Flows of Air and Water," Scientific Reports FZKA 7018, Karlsruhe Institute of Technology (KIT), Karlsruhe (2004)

Gauß, F. and Porombka, P., Internal HZDR Communication, 2015

Hänsch, S., et al., A multi-field two-fluid concept for transitions between different scales of interfacial structures. International Journal of Multiphase Flow, 2012. 47: p. 171-182.

Hewitt, G. F., and N. S. Hall-Taylor, Annular Two-phase Flow, pp. 136-148. Pergamon Press, N. Y. (1970).

Höhne, T. and J.-P. Mehlhoop, 2014, Validation of closure models for interfacial drag and turbulence in numerical simulations of horizontal stratified gas–liquid flows. International Journal of Multiphase Flow. 62(0): p. 1-16.

Höhne, T., Deendarlianto, Lucas, D., 2011. Numerical simulations of counter-current two-phase flow experiments in a PWR hot leg model using an interfacial area density model. Int. J. Heat Fluid Flow 32, 1047–1056.

Höhne, T.; Hänsch, S., A droplet entrainment model for horizontal segregated flows Nuclear Engineering and Design 286(2015), 18-26

Höhne, T.; Geissler, T.; Bieberle, A.; Hampel, U., Numerical modeling of a horizontal annular flow experiment using a droplet entrainment model Annals of Nuclear Energy 77(2015), 351-360

Ishii, M., and M. A. Grolmes,1975, Inception criteria for droplet entrainment in two-phase concurrent film flow, AIChE Journal, Vol. 21, No. 2, p. 308-318.

Ishii, M. and Zuber, N. (1979), Drag coefficient and relative velocity in bubbly, droplet or particulate flows; AIChE Journal Vol. 25(1979)5, 843-855

Ma, J., Oberai, A., Drew, D., Jr, R. L., Hyman, M., 2011. A comprehensive sub-grid air entrainment model for RANS modeling of free surface bubbly flows. JCMF 3, 41-56.

Mayinger, F., Weiss, P., and Wolfert, K. "Two-phase flow phenomena in full-scale reactor geometry," Nuclear Engeneering and Design, 145, 47-61, (1993)

Newitt, D. M., N. Dombrowski, and F. H. Knelman, "Liquid Entrainment: I, The Mechanism of Drop Formation from Gas or Vapor Bubbles, " Trans. Inst. Chem. Eng., 32, 244 (1954).

Prasser, H.-M, Böttger, A., Zschau, J., „A new electrode-mesh tomograph for gas–liquid flows". Flow Measurement and Instrumentation, Vol. 9, pp. 111–119. (1998)

Siddiqui, H., Banerjee S., and Ardon, K.H. "Flooding in an elbow between a vertical and a horizontal or near-horizontal pipe. Part I:Experiments," International Journal of Multiphase Flow, 12, 531-541, (1986)

Stäbler, T.D. „Experimentelle Untersuchung und physikalische Beschreibung der Schichtenströmung in horizontalen Kanälen", Scientific Reports FZKA 7296, Karlsruhe Institute of Technology (KIT), Karlsruhe (2007)

Taitel, Y., and Dukler, A. E. 1976. A model for predicting flow regime transitions in horizontal and near horizontal gas-liquid flow. AIChE J. 22, 47-55.

Vallée, C., Lucas, D., Beyer, M., Pietruske, H., Schütz, P., and Carl, H. 2010 "Experimental CFD grade data for stratified two-phase flows". Nuclear Enginneering and Design, Vol 240, pp. 2347-2356.

Wang, H. and Kondo, S.,"A study on the stratified horizontal counter-current two-phase flow, "Nuclear Engineering and Design,121, 45-52,45, (1990)

Wilcox, D. C. 1994. Turbulence modelling for CFD. La Cañada, California: DCW Industries Inc.

Wintterle, T., "Modellentwicklung und numerische Analyse zweiphasig geschichteter horizontaler Strömungen, "Dissertation, University of Stuttgart, Institute for Nuclear Energy and Energy Systems (IKE), Stuttgart (2008)

Yegorov, Y., Menter, F. 2004. Contact condensation in stratified steam-water flow, EVOL-ECORA –D 07.